COMPEL: The International Journal for Computation and Mathematics in Electrical and Electronic Engineering
DOI: 10.1108/COMPEL-07-2021-0226

Two-Dimensional Steady-State Thermal Analytical Model of Permanent-Magnet Synchronous Machines Operating in Generator Mode

Z. Djelloul-Khedda, K. Boughrara, F. Dubas, G. Baocheng, and A. Ei Hadj

Abstract

Purpose — Thermal analysis of electrical machines is usually performed by using numerical methods or lumped parameter thermal networks (LPTN) depending on the desired accuracy. The analytical prediction of temperature distribution based on the formal resolution of thermal partial differential equations (PDEs) by the harmonic modeling technique (or the Fourier method) is uncommon in electrical machines. Therefore, this paper presents a two-dimensional (2-D) analytical model of steady-state temperature distribution for permanent-magnet (PM) synchronous machines (PMSM) operating in generator mode.

Design/methodology/approach — The proposed model is based on the multi-layer models with the convolution theorem (i.e., Cauchy's product theorem) by using complex Fourier's series and the separation of variables method. This technique takes into the different thermal conductivities of the machine parts. The heat sources are determined by calculating the different power losses in the PMSM with the finite-element method (FEM).

Findings — In order to validate the proposed analytical model, the analytical results are compared with those obtained by thermal FEM. The comparisons show good results of the proposed model.

Originality/value — A new 2-D analytical model based on the PDE in steady-state for full prediction of temperature distribution in the PMSM with taken into account the heat transfer by conduction, convection and radiation.

Keywords: Permanent magnet machine, Thermal analysis, Iron losses, Power losses, Finite element method.

Paper type Research paper

I. Introduction

THE PMSM are becoming important importance in various industries. In recent years, these types of machines are increasingly used in many fields including automotive, aerospace, energy production, household appliances, manufacturing and medical applications. Nowadays, with increasing customer demand for high-torque and high-power densities, highly efficient and small size PMSM, the thermal analysis becomes extremely necessary.

The thermal stress can cause the insulation, the performance degradation and/or the failure of the electrical machine (e.g., reduced efficiency, winding failures or PM demagnetization), hence impact directly on the lifetime of a machine (**Wang *et al*., 2008**; **Li *et al*., 2017**). The heat sources in electrical machines can be classified into three types: i) electrical losses (i.e., Joule losses in the windings), ii) mechanical losses (i.e., friction losses in bearings and in the air-gap), and iii) electromagnetic losses (i.e., iron core and PMs losses). To extend lifetime and protecting the different part of PMSM from high temperature, there are two different ways. The first is to dissipate the losses by cooling and the second is to reduce the losses by optimized electromagnetic design of the electrical machine (**Ghahfarokhi *et al*., 2016**). For this reason, the accurate knowledge of the temperature and heat flow distribution created by the power losses in each part of the machine is very important.

Various tools can be used to analyze the temperature distribution in electrical machines. The most commonly used are numerical methods, such as FEM, or analytical method, such as LPTN. This latter is the most popular method used to estimate the temperature rise in electrical machines. It has the advantage of a fast calculation time. The steady-state thermal model is based on the representation of heat sources and machine materials by a heat generator and thermal resistances respectively. For the transient analysis, heat thermal capacitances are added to consider the temperature variation with time. However, the circuit that accurately models the main heat transfer paths require from the developer to invest some effort to define (**Nasab *et al*., 2020**; **Zhang *et al*., 2021**; **Boglietti *et al*., 2009**). On the other side, FEM are also very often used for thermal analysis of electrical machines. They can be coupled to electromagnetic analysis or directly take the power losses as heat sources (**Chang *et al*., 2017**; **Wang *et al*., 2020**; **Zhang *et al*., 2017**; **Jiang and Jahns 2015**). The main advantage of this numerical method is that any device geometry can be modeled. Moreover, the distribution and the average values of temperatures in all parts of the electrical machine can be obtained and higher accuracy can be given compared with the results of LPTN. Nevertheless, it is very demanding in terms of computational time of the simulations. Indeed, FEM can only be used to model conduction heat transfer in solid components. On the basis of experimental correlations, the radiation and convection must be approximated as boundary conditions (BCs) (**Nategh *et al*., 2012**). In fact, the computational fluid dynamics (CFD) can be also used to calculate the correlation of heat transfer coefficients of each surface between solid and fluid domains (**Nategh *et al*., 2013**; **Yang *et al*., 2017**; **Nategh *et al*., 2019**). Furthermore, multi-physics technique that couples the two numerical methods (i.e., FEM and CFD) is used to take the turbulent flow properties without need

COMPEL: The International Journal for Computation and Mathematics in Electrical and Electronic Engineering
DOI: 10.1108/COMPEL-07-2021-0226

to use heat transfer coefficients as input data in FEM (**Dong *et al.*, 2019**; **Hosain *et al.*, 2017**; **Chong 2019**). This technique is also well known in the field of thermal analysis of electrical machines. It has the distinction of being able to describe the fluid flow. However, next to the very considerable time commitment for simulation and model formation, very powerful computer hardware is required (**Adouni and Cardoso 2019**).

In the thermal analysis of electrical machines, except for the approaches mentioned previously, there are few attempts in previous researches to develop other methods based on the analytical calculation of heat transfer using the formal resolution of thermal PDE. **Buyukdegirmenci *et al.*, (2013a)** developed a closed-form solution (viz., multi-layer model based on Poisson's and Laplace's equations) for the steady-state stator temperature distribution over one slot pitch in a radial air-gap electrical machine. Only two homogeneous layers have been used (i.e., stator lamination and slot/tooth region) where the slot/tooth region was modeled as a homogeneous body with an effective thermal conductivity. The heat source of copper losses is modeled using a heat-flux BC outside of slot/tooth region. In **Buyukdegirmenci *et al.*, (2013b)**, the simplified multi-layer model has been applied to a linear stator structure and has been improved by add more heat-flux BC using horizontal and vertical planar heat sources. **Grobler *et al.*, (2013)** and **Grobler *et al.*, (2015)** presents a 2-D analytical thermal model for a high-speed PMSM. The developed model only allows the temperature to be calculated in a single region inside the PM of the electrical machine. However, the main drawback of the previous approaches is that they cannot consider the different thermal conductivities of the machine parts. Therefore, the analytical prediction of temperature distribution based on the formal resolution of thermal PDE by the harmonic modeling technique (or the Fourier method) is uncommon in electrical machines. To best of the authors' knowledge, there are only two references in the literature that deal with this type of modeling, viz., **Boughrara *et al.*, (2018)** and **Boughrara and Dubas (2021)**, where the authors developed a new 2-D exact analytical for the steady-state heat transfer prediction considering different thermal conductivity in all parts of electrical machines with isotropic or anisotropic materials. It is based on the new subdomain technique developed by **Dubas and Boughrara (2017a)** and **Dubas and Boughrara (2017b)** which was first applied in the electromagnetic field and can take into account the variation of material properties in both directions (e.g., the thermal conductivity in the case of thermal analysis or the magnetic permeability in the case of electromagnetic analysis). This capacity was not available in the conventional subdomain technique (**Dubas and Espanet 2009**; **Boughrara *et al.*, 2012**). However, the model developed in **Dubas and Boughrara (2017a)** and **Dubas and Boughrara (2017b)** does not take into account the heat transfer by radiation and the losses in the stator are calculated uniformly, without calculating separately the losses in the stator teeth and yoke. The same remark can be made for the heat transfer by radiation in **Buyukdegirmenci *et al.*, (2013a)**, **Buyukdegirmenci *et al.*, (2013b)**, **Grobler *et al.*, (2013)** and **Grobler *et al.*, (2015)**.

In this paper, we present a new 2-D thermal analytical model based on the formal resolution of thermal PDE in steady-state for PMSM operating in generator mode. It is based on the multi-layer models with the convolution theorem (i.e., Cauchy's product theorem) by the harmonic modeling technique (or the Fourier method) by applying complex Fourier's series and the separation of variables method (**Sprangers *et al.*, 2016**; **Djelloul-Khedda *et al.*, 2017**; **Djelloul-Khedda *et al.*, 2019**). The developed model takes into account the variation of thermal conductivity in different parts of the electrical machine. In addition to the heat transfer by conductive and convective in the electrical machine, the heat transfer by radiation is also taken into account. It is worthy to point out that the presented method has not been used to develop any thermal model in the literature. The loss determination is carried out by FEM in different parts of the studied machine, where the iron losses are calculated for different parts separately as rotor yoke, stator yoke and teeth. This allows the value and location of heat sources to be well determined. The temperature distribution in all regions of PMSM is predicted with and without the air-gap cooling. Finally, a parametric study was performed to see the temperature change for different parameters. All the results of the proposed analytical model are verified and validated by the thermal FEM (**Meeker, 2010**).

II. MOTOR CONFIGURATION

The PMSM operating in generator mode is shown in **Fig. 1**. It consists of an outer stator with $Q_s = 36$ slots and $q = 3$ phases overlapping winding (viz., the single layer distributed winding), and an inner rotor PM surface-mounted by radially magnetized patterns with $2p = 12$ poles where p is the number of pole pairs. The main dimensions and parameters of the studied machine are given in **Table I**.

COMPEL: The International Journal for Computation and Mathematics in Electrical and Electronic Engineering
DOI: 10.1108/COMPEL-07-2021-0226

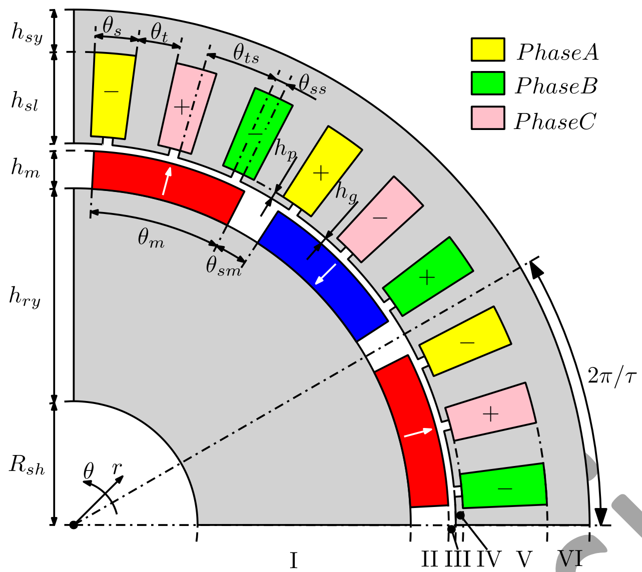

Fig. 1. Studied PMSM (1/4 of the machine).

TABLE I
PARAMETERS OF PMSM.

Symbols	Parameters	Values (Units)
B_r	PMs remanence flux density	1.2 (T)
μ_{rm}	PMs relative permeability	1.02
σ_m	PMs conductivity	0.556E6 (S.m^{-1})
Q_s	Number of stator slots	36
p	Number of pole-pairs	6
R_{sh}	Shaft radius	45 (mm)
h_{ry}	Rotor yoke height	77.8 (mm)
h_m	PMs height	13.7 (mm)
h_g	Air-gap length	2.5 (mm)
h_p	Tooth tips height	3 (mm)
h_{sl}	Stator slot height	30.5 (mm)
h_{sy}	Stator yoke height	15.5 (mm)
L_u	Axial length	310 (mm)
θ_s	Axial length	5 (°)
θ_t	Stator teeth angle	5 (°)
θ_{ss}	Stator slot opening angle	1.5 (°)
θ_{ts}	Stator teeth tips angle	7.2 (°)
θ_m	PMs opening angle	24 (°)
θ_{sm}	Angle of air space between PMs	6 (°)
Ω_{me}	Mechanical speed	500 (rpm)
R_s	Stator resistance	53.19E-3 (Ω)
F	Stator fill factor	0.29
N_c	Number of conductors of slot coil	11

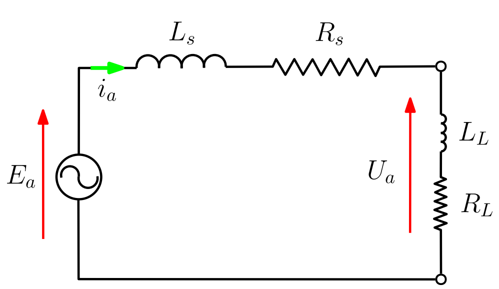

Fig. 2. Single-phase electrical equivalent circuit.

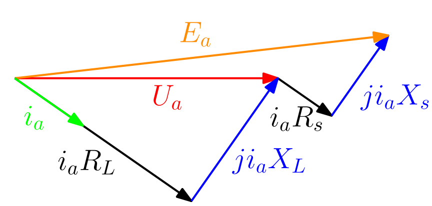

Fig. 3. Single-phase phasor diagram.

III. Electromagnetic Performances

The prediction of the integral quantities allows the electromagnetic performance evaluation of PMSM. Moreover, this performance is affected and simultaneously affects the temperature in electrical machines.

A. *Electric Power Calculation*

The electric power generated by the PMSM is calculated as

$$P_e = \frac{1}{T}\int_T R_L[i_a^2(t) + i_b^2(t) + i_c^2(t)]dt \tag{1}$$

where R_L is the load resistance, T is the electrical period, and $\{i_a, i_b, i_c\}$ are the phase currents.

B. *Electromagnetic Torque Calculation*

According to the Maxwell stress tensor, the electromagnetic torque T_{em} is computed by

$$T_{em}(t) = \frac{L_u R_g^2}{\mu_0}\int_0^{2\pi} B_r^{airg}(R_g, \theta, t) B_\theta^{airg}(R_g, \theta, t) d\theta \tag{2}$$

where μ_0 is the vacuum permeability, L_u is the axial length of the electrical machine, $R_g = (R_3 + R_4)/2$ is the average radius in the air-gap, and B_r^{airg} & B_θ^{airg} are respectively the radial and tangential components of the magnetic flux density in the air-gap.

C. *Mechanical Power Calculation*

The PMSM mechanical power is calculated by

$$P_{me}(t) = \frac{2\pi\Omega_{me}}{60}|T_{em}(t)| \tag{3}$$

where Ω_{me} is the mechanical speed.

D. *Back Electromotive Force (EMF) Calculation*

The single-phase back EMF, i.e., E_a, can be computed as

$$E_a = -\frac{N_c L_u}{S}\left(\iint_{\Omega^+} \frac{\partial A}{\partial t} d\Omega - \iint_{\Omega^-} \frac{\partial A}{\partial t} d\Omega\right) \tag{4}$$

where N_c is the number of conductors of slot coil, S is the conductor area of each turn of phase winding, A is the magnetic vector potential component along the z-axis, and Ω^+ & Ω^- are respectively the cross-sectional areas of '*go*' and '*return*' conductor of the coil.

E. *Voltages and Currents Calculation*

The stator phase circuit equation can be obtained from the single-phase electrical equivalent circuit shown in **Fig. 2** by

$$U_a = E_a - R_s i_a - L_s \frac{di_a}{dt} = R_L i_a + L_L \frac{di_a}{dt} \tag{5}$$

where R_s is the stator resistance, L_s and L_L are respectively the stator and load inductance, and U_a is the voltage of one phase.

According to single-phase phasor diagram shown in **Fig. 3**, **(5)** can be given by

$$U_a(t) \approx E_a - R_s i_a - jX_s i_a = R_L i_a + jX_L i_a \tag{6}$$

where X_s and X_L are respectively the stator and the load impedance given by

$$X_s = p\omega_r L_s \tag{7}$$

$$X_L = p\omega_r L_L \tag{8}$$

where ω_r is the rotor speed in (rad/s).

From **(6)**, we can obtain the currents of one phase by

$$i_a = \frac{E_a}{R_s + R_L + j(X_s + X_L)} \tag{9}$$

IV. LOSS CALCULATION

Losses in electrical machines are an important part of the electromagnetic performance evaluation. Moreover, these losses directly affect the efficiency and are the main source of heat generation in these machines. However, in our case, because the low-speed of rotor, the friction losses in the air-gap is neglected.

A. Iron Core Loss Calculation

For a no-sinusoidal excitation and according to **Bertotti's (1988)** model, the iron core loss calculation, i.e., P_{iron}, in the PMSM can be expressed by

$$\begin{aligned} P_{iron} &= P_{hys} + P_{edd} + P_{ex} \\ &= k_h \frac{1}{T} B_m^2 C_f + k_{ed} \frac{1}{T} \int_T \left(\frac{dB}{dt}\right)^2 dt + k_{ex} \frac{1}{T} \int_T \left|\frac{dB}{dt}\right|^{1.5} dt \end{aligned} \tag{10}$$

where P_{hys}, P_{edd}, and P_{ex} are respectively the hysteresis, eddy-current and excess losses; B is the iron core magnetic density; B_m is the peak value of the magnetic flux density in the iron core; T is the iron core magnetic flux density period; k_h, k_{ed}, and k_{ex} are respectively the coefficient of hysteresis, eddy-current and excess losses. The eddy-current losses coefficient and the correction factor C_f used to take the total loss depend on the magnitude of every local minor loops are given by

$$k_{ed} = \frac{\sigma_{iron} d^2}{12} \tag{11}$$

$$C_f = 1 + \frac{0.65}{B_m} \sum_{i=1}^{N_i} \Delta B_i \tag{12}$$

where σ_{iron} is the electrical conductivity; d is the lamination thickness; N_i is the number of hysteresis loops, and ΔB_i is the magnitude of i^{th} hysteresis loop.

B. PMs Loss Calculation

In general, the 3-D PMs eddy-current losses can be expressed by **Benlamine *et al.*, (2015)**

$$P_m = \int_V \mathbf{J}^2/\sigma_m \, dV \tag{13}$$

where **J** is the resultant eddy-current density, σ_m is the electrical conductivity of PMs, and V is the PMs volume.

C. Winding Loss Calculation

The copper loss in the stator winding is calculated as

$$P_{sl} = \frac{1}{T} \int_T R_s [i_a^2(t) + i_b^2(t) + i_c^2(t)] dt \tag{14}$$

D. Principal Quantities and Power Loss Results

The extracted parameters values of the studied machine are calculated at Ω_{me} with an electric load $\{R_L = 2.22\,\Omega$ & $L_L = 3.22\,mH\}$ [see **Fig. 2**]. Using the dimensions/parameters of the studied machine and the coefficients of M800-65A (i.e., laminated steel core) given in **Table I** and **II** respectively. The main quantities of the machine performance are calculated based on the FEM and summarized in **Table III**. The iron core losses are calculated in different parts of the electrical machine, viz.: rotor/stator yoke and teeth losses. The results of different type of power losses will be used as input data for the developed analytical thermal model.

TABLE II
IRON LOSS COEFFICIENTS OF M800-65A.

Symbols	Parameters	Values (Units)
k_{hys}	Hysteresis losses coefficient	225.252 (W.s.T$^{-\alpha}$.m^{-3})
k_{ex}	Excess loss coefficient	1.414E-1 (W.s$^{1.5}$.T$^{-1.5}$.m^{-3})
α	Steinmetz constant	2
σ_{iron}	Conductivity	3.546E6 (S.m^{-1})
d_l	Lamination thickness	0.65 (mm)
ρ	Lamination mass density	7.8E3 (kg.m^{-3})

COMPEL: The International Journal for Computation and Mathematics in Electrical and Electronic Engineering
DOI: 10.1108/COMPEL-07-2021-0226

TABLE III
EXTRACTED PARAMETERS OF PMSM.

Symbols	Parameters	Values (Units)
i_{abc}	RMS phase current	80.33 (A)
U_{abc}	RMS phase tension	200 (V)
T_{em}	Electromagnetic torque	870.11 (N.m)
P_{me}	Mechanical power	45.559 (kW)
P_e	Electrical power	42.862 (kW)
P_{ry}	Rotor yoke losses	48.43E-3 (W)
P_m	PMs losses	17.74 (W)
P_{sl}	Stator slot losses	1.03 (kW)
P_t	Stator teeth losses	344.69 (W)
P_{sy}	Stator yoke losses	288.56 (W)
P_{loss}	Total power losses	1.68 (kW)

V. THERMAL ANALYTICAL MODELING

A. Problem Formulation and Assumptions

The model is formulated in a 2-D polar coordinate system. The problem can be divided into $\tau = 2p$, then, the periodicity of the problem is $2\pi/\tau$ with six regions (i.e., layers) as shown in **Fig. 1**, viz.,

- Regions I and VI: the rotor and stator yoke;
- Region II: the PMs and the air-space between PMs;
- Region III: the air-gap;
- Region IV: the stator isthmus-opening and tooth-tips;
- Region V: the stator slots and teeth.

The angular position of the i^{th} stator slot-opening and l^{th} PMs are defined respectively by

$$\alpha_i = \frac{2\pi}{Q_s} i - \frac{\pi}{Q_s} \tag{15}$$

$$\gamma_l = \frac{\pi}{p} l - \frac{\pi}{p} \tag{16}$$

with $1 \leq i \leq Q_s$ and $1 \leq l \leq 2p$.

The model is formulated with the following assumptions:

- Interfaces between regions are assumed to be perfect;
- Heat sources are uniform and constant;
- Materials are considered isotropic having constant thermal conductivities without any variation with temperature;
- Stator and rotor slots/teeth have radial sides;
- The axial length of the machine is considered infinite and invariant (i.e., the end-effects are neglected);
- The thermal conductivity in regions is spatially invariant in the radial direction, but can be spatially variant in the tangential direction.

B. Heat Source and Thermal Conductivity Distribution

The heat power source density P can be cc by

$$P(\theta) = \sum_{n=-\infty}^{\infty} \hat{P}_n \, e^{-jn\tau\theta} \tag{17}$$

where $j = \sqrt{-1}$, $n \in]-\infty, +\infty[$ is spatial harmonic orders. Practically, we develop **(17)** and the all following expressions which will be presented in complex Fourier series expansion to a certain rank harmonic N where $n \in [-N, +N]$. $\hat{P}_n$ is the complex Fourier coefficient defined by

COMPEL: The International Journal for Computation and Mathematics in Electrical and Electronic Engineering
DOI: 10.1108/COMPEL-07-2021-0226

$$\hat{P}_n = \begin{cases} \sum_{i=1}^{Q/\tau} \frac{1}{2\pi jn}\left[P_T e^{-jn\tau\frac{\theta_S}{2}}\left(1-e^{-jn\tau\theta_T}\right)+2jP_S \sin\left(\frac{n\tau\theta_S}{2}\right)\right]e^{jn\tau\alpha_i}, & n \neq 0 \\ \frac{Q}{2\pi}(P_T\theta_T + P_S\theta_S), & n = 0 \end{cases} \quad (18)$$

where $\{Q, P_T, P_S, \theta_T, \theta_S, \alpha_i, i\}$ are replaced by region according to **Table IV**. In this table, $\{V_{ry}, V_m, V_a, V_t, V_{sl}, V_{sy}\}$ are the volumes of different parts of source heat given in **Appendix A**. All coefficients of $\hat{P}_n$ are grouped together in one column vector **P** as

$$\mathbf{P} = [\hat{P}_{-N} \quad \cdots \quad \hat{P}_N]^T \quad (19)$$

The thermal conductivity distribution is given in terms of the complex Fourier series decomposition by

$$\lambda(\theta) = \sum_{n=-\infty}^{\infty} \hat{\lambda}_n \, e^{-jn\tau\theta} \quad (20)$$

$$\lambda^{inv}(\theta) = \sum_{n=-\infty}^{\infty} \hat{\lambda}_n^{inv} \, e^{-jn\tau\theta} \quad (21)$$

where $\hat{\lambda}_n$ is the complex Fourier coefficient defined by

$$\hat{\lambda}_n = \begin{cases} \sum_{i=1}^{Q/\tau} \frac{1}{2\pi jn}\left[\lambda_T e^{-jn\tau\frac{\theta_S}{2}}\left(1-e^{-jn\tau\theta_T}\right)+2j\lambda_S \sin\left(\frac{n\tau\theta_S}{2}\right)\right]e^{jn\tau\alpha_i}, & n \neq 0 \\ \frac{Q}{2\pi}(\lambda_T\theta_T + \lambda_S\theta_S), & n = 0 \end{cases} \quad (22)$$

where $\{\lambda_T, \lambda_S\}$ are given to **Table IV** according to the region. To calculate $\hat{\lambda}_n^{inv}$, we replaced $\{\lambda_T \ \& \ \lambda_S\}$ by $\{1/\lambda_T, 1/\lambda_S\}$ in **(22)**.

TABLE IV
COMPLEX FOURIER COEFFICIENTS PARAMETERS OF HEAT SOURCE AND THERMAL CONDUCTIVITY.

Regions	Q	P_T	P_S	λ_T	λ_S	θ_T	θ_S	α_i	i
I	$2p$	P_{ry}/V_{ry}	P_{ry}/V_{ry}	λ_r	λ_r	θ_{tm}	θ_m	γ_l	l
II	$2p$	P_m/V_m	0	λ_m	λ_e	θ_m	θ_{sm}	γ_l	l
III	$2p$	P_{co}/V_a	P_{co}/V_a	λ_a	λ_a	θ_{tm}	θ_m	γ_l	l
IV	Q_s	P_t/V_t	0	λ_s	λ_e	θ_{ts}	θ_{ss}	α_i	i
V	Q_s	P_t/V_t	P_{sl}/V_{sl}	λ_s	λ_{sl}	θ_t	θ_s	α_i	i
VI	Q_s	P_{sy}/V_{sy}	P_{sy}/V_{sy}	λ_s	λ_s	θ_t	θ_s	α_i	i

Fig. 4 shows the thermal conductivity and heat source distribution in all parts of PMSM developed by complex Fourier series presented in **(18)** and **(22)**. The distribution of these components is compared with those of FEM [see **Fig. 4**] and will be used for the development of the thermal analytical model.

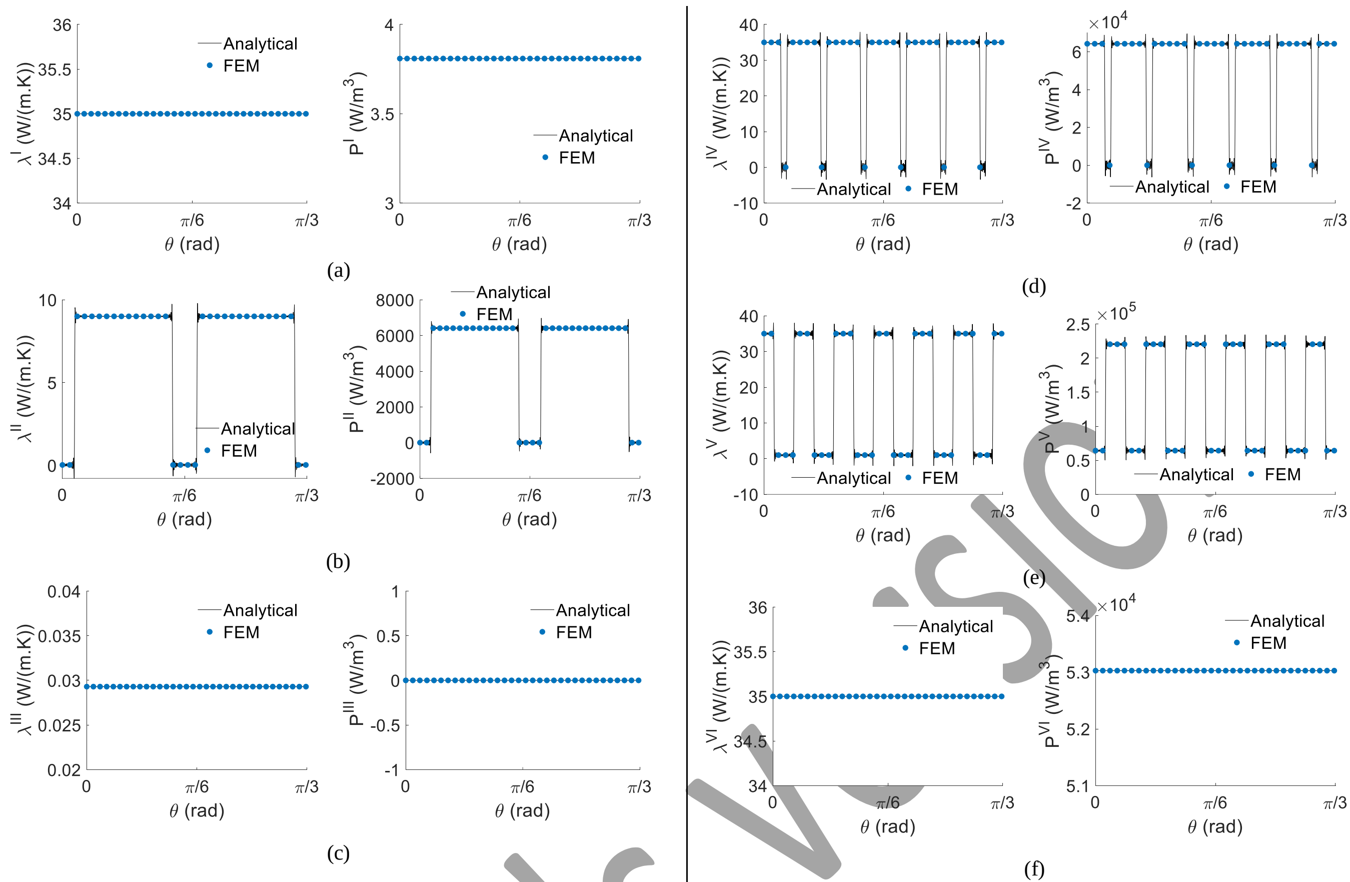

Fig. 4. Thermal conductivity distribution in left side and heat source distribution in right side for region (a) I, (b) II, (c) III, (d) IV, (e) V and (f) VI.

C. Analytical Temperature Calculation

In steady-state, the thermal PDE of the temperature distribution are given by the following Poisson's equation:

$$\nabla^2 T = -\frac{1}{\lambda} P \tag{23}$$

where T and λ are respectively the temperature and the thermal conductivity. In terms of the complex Fourier series decomposition, the temperature distribution is given by

$$T(r,\theta) = \sum_{n=-\infty}^{\infty} \hat{T}_n(r)\, e^{-jn\tau\theta} \tag{24}$$

The basic law that defines the relation between the temperature gradient ∇T and the heat-flux density q is Fourier's law given in the next form

$$q = -\lambda . \nabla T \tag{25}$$

Using **(25)**, the components of heat-flux density are obtained as follows:

$$q_r = -\lambda \frac{\partial T}{\partial r} \tag{26}$$

$$q_\theta = -\frac{\lambda}{r} \frac{\partial T}{\partial \theta} \tag{27}$$

In complex Fourier terms

$$q_r(r,\theta) = \sum_{n=-\infty}^{\infty} \hat{q}_{r,n}(r)\, e^{-jn\tau\theta} \tag{28}$$

DOI: 10.1108/COMPEL-07-2021-0226

$$q_\theta(r,\theta) = \sum_{n=-\infty}^{\infty} \hat{q}_{\theta,n}(r)\, e^{-jn\tau\theta} \tag{29}$$

By using the Cauchy's product theorem and the complex Fourier series decomposition (**Sprangers *et al.*, 2016**; **Djelloul-Khedda *et al.*, 2017; Djelloul-Khedda *et al.*, 2019**) in **(26)** - **(27)**, we obtain

$$\sum_{m=-N}^{N} \hat{\lambda}_{n-m}^{inv}\, \hat{q}_{r,m} = -\frac{\partial \hat{T}_n}{\partial r} \tag{30}$$

$$\sum_{m=-N}^{N} \hat{\lambda}_{n-m}^{inv}\, \hat{q}_{\theta,m} = -\frac{1}{r}\frac{\partial \hat{T}_n}{\partial r} \tag{31}$$

in matrix form **(31)** - **(32)** given by

$$\mathbf{q}_r = -\boldsymbol{\lambda}_c \frac{\partial \mathbf{T}}{\partial r} \tag{32}$$

$$\mathbf{q}_\theta = j\frac{1}{r}\boldsymbol{\lambda}_c\, \mathbf{N}_\tau \mathbf{T} \tag{33}$$

where $\boldsymbol{\lambda}_c$ is the convolution matrices of thermal conductivity given by

$$\boldsymbol{\lambda}_c = \begin{bmatrix} \hat{\lambda}_0^{inv} & \cdots & \hat{\lambda}_{-2N}^{inv} \\ \vdots & \ddots & \vdots \\ \hat{\lambda}_{2N}^{inv} & \cdots & \hat{\lambda}_0^{inv} \end{bmatrix}^{-1} \tag{34}$$

or by

$$\boldsymbol{\lambda}_c = \begin{bmatrix} \hat{\lambda}_0 & \cdots & \hat{\lambda}_{-2N} \\ \vdots & \ddots & \vdots \\ \hat{\lambda}_{2N} & \cdots & \hat{\lambda}_0 \end{bmatrix} \tag{35}$$

and $\mathbf{N}_\tau$ is the diagonal matrix of $\overline{\mathbf{N}}_{\boldsymbol{\tau}}$, viz.,

$$\mathbf{N}_\tau = diag[\overline{\mathbf{N}}_{\boldsymbol{\tau}}] \tag{36}$$

$$\overline{\mathbf{N}}_{\boldsymbol{\tau}} = \tau.[-N \cdots N] \tag{37}$$

In matrix form **(24)**, **(28)** and **(29)** can be written by

$$T(r,\theta) = [\mathbf{T}|_r]^T.[\mathbf{E}_{\boldsymbol{\tau}}|_\theta]^T \tag{38}$$

$$q_r(r,\theta) = [\mathbf{q}_r|_r]^T.[\mathbf{E}_{\boldsymbol{\tau}}|_\theta]^T \tag{39}$$

$$q_\theta(r,\theta) = [\mathbf{q}_\theta|_r]^T.[\mathbf{E}_{\boldsymbol{\tau}}|_\theta]^T \tag{40}$$

with

$$\mathbf{T}|_r = [\hat{T}_{-N}(r) \quad \cdots \quad \hat{T}_N(r)]^T \tag{41}$$

$$\mathbf{q}_r|_r = \left[\hat{q}_{r_{-N}}(r) \quad \cdots \quad \hat{q}_{r_N}(r)\right]^T \tag{42}$$

$$\mathbf{q}_\theta|_r = \left[\hat{q}_{\theta_{-N}}(r) \quad \cdots \quad \hat{q}_{\theta_N}(r)\right]^T \tag{43}$$

$$\mathbf{E}_{\boldsymbol{\tau}}|_\theta = e^{-j\overline{\mathbf{N}}_{\boldsymbol{\tau}}\theta} \tag{44}$$

D. Thermal PDE in each Region

The temperature distribution in all regions is calculated from **(23)** by solving the following Poisson's matrix equations:

$$\frac{\partial^2 \mathbf{T}^K|_r}{\partial r^2} + \frac{1}{r}\frac{\partial \mathbf{T}^K|_r}{\partial r} - \left(\frac{\mathbf{V}^K}{r}\right)^2 \mathbf{T}^K|_r = -[\boldsymbol{\lambda}_c^K]^{-1}\mathbf{p}^K \tag{45}$$

with $\mathbf{V}^K = ([\boldsymbol{\lambda}_c^K]^{-1}\mathbf{N}_{\boldsymbol{\tau}}\, \boldsymbol{\lambda}_c^K \mathbf{N}_{\boldsymbol{\tau}})^{\frac{1}{2}}$ where K is the index of regions in the lettering ($\boldsymbol{sym}^K$: K = **I**, **II**, . . . **VI**).

Using the separation of variables method in (r,θ), the general solution of **(45)** is formulated as

$$\mathbf{T}^K|_r = \mathbf{W}^K\left(\frac{r}{R_{k+1}}\right)^{\mathbf{L}^K}\mathbf{a}^K + \mathbf{W}^K\left(\frac{R_k}{r}\right)^{\mathbf{L}^K}\mathbf{b}^K + r^2\mathbf{F}^K \tag{46}$$

The index k represent the radius of different machine parts, in the lettering ($\boldsymbol{sym}_k$: k = 1, 2, . . . 7), where R_k: $\{R_1$ to $R_7\}$ are given in **Appendix B**. The matrices $\mathbf{L}^K$ and $\mathbf{W}^K$ are respectively the diagonal eigenvalue and the eigenvector matrix of $\mathbf{V}^K$, the vectors $\mathbf{a}^K$ & $\mathbf{b}^K$ are the column vectors of the constant's unknown coefficients, and the term $r^2\mathbf{F}^K$ represents the particular solution of **(45)** with

$$\mathbf{F}^K = ([\mathbf{V}^K]^2 - 4\mathbf{I})^{-1}[\boldsymbol{\lambda}_c^K]^{-1}\mathbf{p}^K \tag{47}$$

where $\mathbf{I}$ is a diagonal identity matrix with same size as $\mathbf{N}_\tau$.

From **(32)**, **(33)** and **(46)**, the matrix equation of heat-flux density $\{\mathbf{q}_r;\ \mathbf{q}_\theta\}$ in the different regions are given by

$$\mathbf{q}_r^K|_r = -\frac{1}{r}\left[\boldsymbol{\lambda}_c^K\mathbf{W}^K\mathbf{L}^k\left(\frac{r}{R_{k+1}}\right)^{\mathbf{L}^K}\mathbf{a}^K - \boldsymbol{\lambda}_c^K\mathbf{W}^K\mathbf{L}^K\left(\frac{R_k}{r}\right)^{\mathbf{L}^K}\mathbf{b}^K + 2r^2\boldsymbol{\lambda}_c^K\mathbf{F}^K\right] \tag{48}$$

$$\mathbf{q}_\theta{}^K|_r = \frac{j}{r}\left[\boldsymbol{\lambda}_c^K\mathbf{N}_\tau\mathbf{W}^K\left(\frac{r}{R_{k+1}}\right)^{\mathbf{L}^K}\mathbf{a}^K + \boldsymbol{\lambda}_c^K\mathbf{N}_\tau\mathbf{W}^K\left(\frac{R_k}{r}\right)^{\mathbf{L}^K}\mathbf{b}^K + r^2\boldsymbol{\lambda}_c^K\mathbf{N}_\tau\mathbf{F}^K\right] \tag{49}$$

E. Definition of BCs

When considering heat transfer inside the machine by conduction, the BCs between two adjacent media are given as follows

$$\mathbf{T}^{K-1}|_{r=R_k} - \mathbf{T}^K|_{r=R_k} = 0 \tag{50}$$

$$\mathbf{q}_r^{K-1}|_{r=R_k} - \mathbf{q}_r^K|_{r=R_k} = 0 \tag{51}$$

where $K \in [\mathbf{II},\mathbf{VI}]$ and $k \in [2,6]$.

Inside the rotor and outside the stator, the BCs due to the heat transfer by convection and radiation can be mathematically written as

$$\mathbf{q}_r^I|_{r=R_1} = -h_r\left(\mathbf{T}^I|_{r=R_1} - \mathbf{T}_{int}\right) - \varepsilon_r\sigma\left(\mathbf{T}^{I^4}\Big|_{r=R_1} - \mathbf{T}_{int}{}^4\right) \tag{52}$$

$$\mathbf{q}_r^{VI}|_{r=R_7} = h_s\left(\mathbf{T}^{VI}|_{r=R_7} - \mathbf{T}_{ext}\right) + \varepsilon_s\sigma\left(\mathbf{T}^{VI^4}\Big|_{r=R_7} - \mathbf{T}_{ext}{}^4\right) \tag{53}$$

where $\{h_r;\ h_s\}$ and $\{\varepsilon_r;\ \varepsilon_s\}$ are respectively the convection and the emissivity coefficient inside the rotor and outside the stator, σ is Boltzmann's constant, $\{\mathbf{T}_{int};\ \mathbf{T}_{ext}\}$ are the temperature column vectors of vacuum in the rotor shaft and outside the machine given in **Appendix C**.

Both **(52)** and **(53)** are fourth degree equations and cannot be applied in the presented modeling, then we have to change them by applying the following equality **Ghahfarokhi *et al.*, (2016**) and **0)**

$$\varepsilon_r\sigma\left(\mathbf{T}^{I^4}\Big|_{r=R_1} - \mathbf{T}_{int}{}^4\right) = h_{r,ra}\left(\mathbf{T}^I|_{r=R_1} - \mathbf{T}_{int}\right) \tag{54}$$

$$\varepsilon_s\sigma\left(\mathbf{T}^{VI^4}\Big|_{r=R_7} - \mathbf{T}_{ext}{}^4\right) = h_{s,ra}\left(\mathbf{T}^{VI}|_{r=R_7} - \mathbf{T}_{ext}\right) \tag{55}$$

where $\{h_{r,ra}\&\ h_{s,ra}\}$ are the radiation coefficient inside the rotor and outside the stator respectively. From **(54)** and **(55)**, we have

$$h_{r,ra} = \mathbf{mean}\left[\varepsilon_r\sigma\left(T^I(R_1,\theta)^2 + T_{int}{}^2\right)\left(T^I(R_1,\theta) + T_{int}\right)\right] \tag{56}$$

$$h_{s,ra} = \mathbf{mean}\left[\varepsilon_s\sigma\left(T^{VI}(R_7,\theta)^2 + T_{ext}{}^2\right)\left(T^{VI}(R_7,\theta) + T_{ext}\right)\right] \tag{57}$$

In fact, $\{h_{r,ra}\&\ h_{s,ra}\}$ are varied depending on the θ-direction, because the temperature inside the rotor and outside the stator is almost constant. We take the mean values as indicated in **(56)** and **(57)**. Then, **(52)** and **(53)** will be

$$\mathbf{q}_r^I|_{r=R_1} = -h_{r,eq}\left(\mathbf{T}^I|_{r=R_1} - \mathbf{T}_{int}\right) \tag{58}$$

DOI: 10.1108/COMPEL-07-2021-0226

$$\mathbf{q}_r^{VI}|_{r=R_7} = h_{s,eq}\left(\mathbf{T}^{VI}|_{r=R_7} - \mathbf{T}_{ext}\right) \tag{59}$$

where $\{h_{r,eq} \& \, h_{s,eq}\}$ are the equivalent convection-radiation coefficient inside the rotor and outside the stator given by

$$h_{r,eq} = h_r + h_{r,ra} \tag{60}$$

$$h_{s,eq} = h_s + h_{s,ra} \tag{61}$$

At $r = R_k$ where $k \in [2,6]$ and $K \in [\mathbf{II}, \mathbf{VI}]$, **(46)**, **(48)**, **(50)**, and **(51)** give

$$\mathbf{W}^{K-1}\mathbf{a}^{K-1} + \mathbf{W}^{K-1}\left(\frac{R_{k-1}}{R_k}\right)^{\mathbf{L}^{K-1}}\mathbf{b}^{K-1} - \mathbf{W}^{K}\left(\frac{R_k}{R_{k+1}}\right)^{\mathbf{L}^{K}}\mathbf{a}^{K} - \mathbf{W}^{K}\mathbf{b}^{K} = (-\mathbf{F}^{K-1} + \mathbf{F}^{K})R_k^{\ 2} \tag{62}$$

$$\boldsymbol{\lambda}_c^{K-1}\mathbf{W}^{K-1}\mathbf{L}^{K-1}\mathbf{a}^{K-1} - \boldsymbol{\lambda}_c^{K-1}\mathbf{W}^{K-1}\mathbf{L}^{K-1}\left(\frac{R_{k-1}}{R_k}\right)^{\mathbf{L}^{K-1}}\mathbf{b}^{K-1} - \boldsymbol{\lambda}_c^{K}\mathbf{W}^{K}\mathbf{L}^{K}\left(\frac{R_k}{R_{k+1}}\right)^{\mathbf{L}^{K}}\mathbf{a}^{K} + \boldsymbol{\lambda}_c^{K}\mathbf{W}^{K}\mathbf{L}^{K}\mathbf{b}^{K} = 2(-\boldsymbol{\lambda}_c^{K-1}\mathbf{F}^{K-1} + \boldsymbol{\lambda}_c^{K}\mathbf{F}^{K})R_k^{\ 2} \tag{63}$$

At $r = R_1$, **(46)**, **(48)** and **(58)** give

$$\left(h_{r,eq}\mathbf{W}^{I} - \left(\frac{1}{R_1}\right)\boldsymbol{\lambda}_c^{I}\mathbf{W}^{I}\mathbf{L}^{I}\right)\left(\frac{R_1}{R_2}\right)^{\mathbf{L}^{I}}\mathbf{a}^{I} + \left(h_{r,eq}\mathbf{W}^{I} + \left(\frac{1}{R_1}\right)\boldsymbol{\lambda}_c^{I}\mathbf{W}^{I}\mathbf{L}^{I}\right)\mathbf{b}^{I} = \left(2\boldsymbol{\lambda}_c^{I} - h_{r,eq}R_1\mathbf{I}\right)R_1\mathbf{F}^{I} + h_{r,eq}\mathbf{T}_{int} \tag{64}$$

At $r = R_7$, **(46)**, **(48)** and **(59)** give

$$\left(-h_{s,eq}\mathbf{W}^{VI} - \left(\frac{1}{R_7}\right)\boldsymbol{\lambda}_c^{VI}\mathbf{W}^{I}\mathbf{L}^{VI}\right)\mathbf{a}^{VI} + \left(-h_{s,eq}\mathbf{W}^{VI} + \left(\frac{1}{R_7}\right)\boldsymbol{\lambda}_c^{VI}\mathbf{W}^{VI}\mathbf{L}^{VI}\right)\left(\frac{R_6}{R_7}\right)^{\mathbf{L}^{VI}}\mathbf{b}^{VI} = \left(2\boldsymbol{\lambda}_c^{VI} + h_{s,eq}R_1\mathbf{I}\right)R_7\mathbf{F}^{VI} - h_{s,eq}\mathbf{T}_{ext} \tag{65}$$

The system of 12 BCs matrix equations **(62)** ~ **(65)** permits to determine the coefficients of temperature in the all regions of PMSM. All coefficients and BCs matrix equations are collected in matrix under the form $\mathbf{X} = \mathbf{A^{-1}} \,.\, \mathbf{Y}$ where $\mathbf{X}$, $\mathbf{A}$, and $\mathbf{Y}$ represent respectively the column vectors of unknown coefficients, the coefficient factor matrix and the column vectors of the constant values in the BCs equations.

F. Dissipative Heat Power Calculation

The dissipative heat power (i.e., total heat flux) outside the stator P_{ext} and inside the rotor P_{int} are calculated by

$$P_{ext} = L_u R_7 \int_0^{2\pi} q^{VI}(R_7, \theta)\, d\theta \tag{66}$$

$$P_{int} = L_u R_1 \int_0^{2\pi} q^{I}(R_1, \theta)\, d\theta \tag{67}$$

where

$$q^{VI}(R_7, \theta) = \sqrt{q_r^{VI}(R_7, \theta)^2 + q_\theta^{VI}(R_7, \theta)^2} \tag{68}$$

$$q^{I}(R_1, \theta) = \sqrt{q_r^{I}(R_1, \theta)^2 + q_\theta^{I}(R_1, \theta)^2} \tag{69}$$

G. Algorithmic Solution

Fig. 5 shows the steps to obtain the temperature distribution in the PMSM by an iterative procedure. In the first step, the temperature distribution is calculated without considering the heat transfer by radiation. Then, the radiation coefficients are calculated from the inside and outside (i.e., ambient) temperature of PMSM by using **(56)** to **(57)**. In the next step, the calculation of temperature distribution is performed taking into account the heat transfer by radiation. In the algorithmic, the term ξ represents the maximum allowable error to achieve convergence of solution.

COMPEL: The International Journal for Computation and Mathematics in Electrical and Electronic Engineering
DOI: 10.1108/COMPEL-07-2021-0226

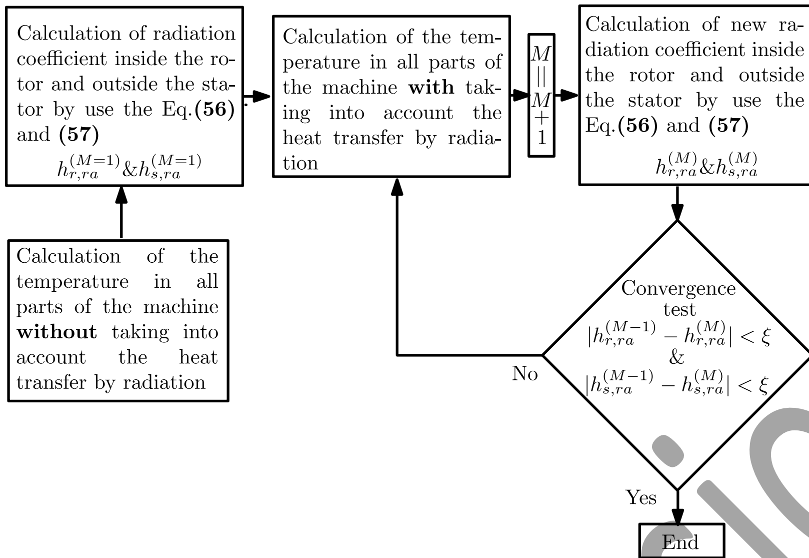

Fig. 5. Algorithmic solution.

VI. RESULTS AND VALIDATION

The main dimensions and parameters of PMSM are given in **Table I.** The power losses, used as sources for the thermal model, are given in **Table III**. The thermal conductivities, ambient temperatures, convection and emissivity coefficients used in the thermal model are listed in **Table V** where forced air cooling is applied to the outside of the stator**.**

The computation time requirements for the temperature calculation in the PMSM and the root-mean-square (RMS) error of the temperateure in the middle of the air gap are shown in **Table VI**. In the developed model, for $N = 120$, which represent the optimal value with an acceptable RMS error and a small calculation time, the the resulting system of equations has $2.\left[(2N + 1).6_{regions}\right] =$ 2,892 unknown coefficients with $\xi = 0.1$. For the FEM, we have 26,750 domain elements and 2,748 boundary elements.The RMS error is calculated with $Ms = 500$ points as

$$\text{RMS error} = \frac{1}{M_s}\sum_{m=1}^{M_s}\left|T_m^{FEM} - T_m^{AM}\right| \tag{70}$$

where T_m^{FEM} and T_m^{AM} are the temperatures of a point on the air-gap by FEM and the devloped analytical model respectivly.

TABLE V
PARAMETERS OF THE THERMAL MODEL.

Symbols	Parameters	Values (Units)
λ_e	Vacuum thermal conductivity	2.9E-2 (W/m/K)
λ_a	Air-gap thermal conductivity	2.93E-2 (W/m/K)
λ_m	PMs thermal conductivity	9 (W/m/K)
λ_{M800}	M800-65A thermal conductivity	35 (W/m/K)
λ_s	Stator iron thermal conductivity	λ_{M800}
λ_r	Rotor iron thermal conductivity	λ_{M800}
λ_{sl}	Stator slot thermal conductivity	1 (W/m/K)
h_r	Convection coefficient inside the rotor	3 (W/m^2/K)
h_s	Convection coefficient outside the stator	105 (W/m^2/K)
ε_r	Emissivity coefficient inside the rotor	0.2
ε_s	Emissivity coefficient outside the stator	0.8
σ	Stefan–Boltzmann constant	5.670367E-8
T_{int}	Temperature inside the rotor	25 (°C)
T_{ext}	Temperature outside the stator	20 (°C)
ν_0	Air kinematic viscosity	20.96E-6 (m^2/s)

COMPEL: The International Journal for Computation and Mathematics in Electrical and Electronic Engineering
DOI: 10.1108/COMPEL-07-2021-0226

TABLE VI
COMPUTATION TIMES AND RMS ERROR.

	Analytical Model										FEM
N	**20**	**40**	**60**	**80**	**100**	**120**	**140**	**160**	**180**	**200**	
Time [sec]	0.41	1.01	2.02	3.35	4.08	5.95	9.93	14.53	19.96	25.79	14
RMS error (m°C)	141.16	64.01	42.37	33.38	29.65	29.13	28.90	28.88	28.85	28.83	

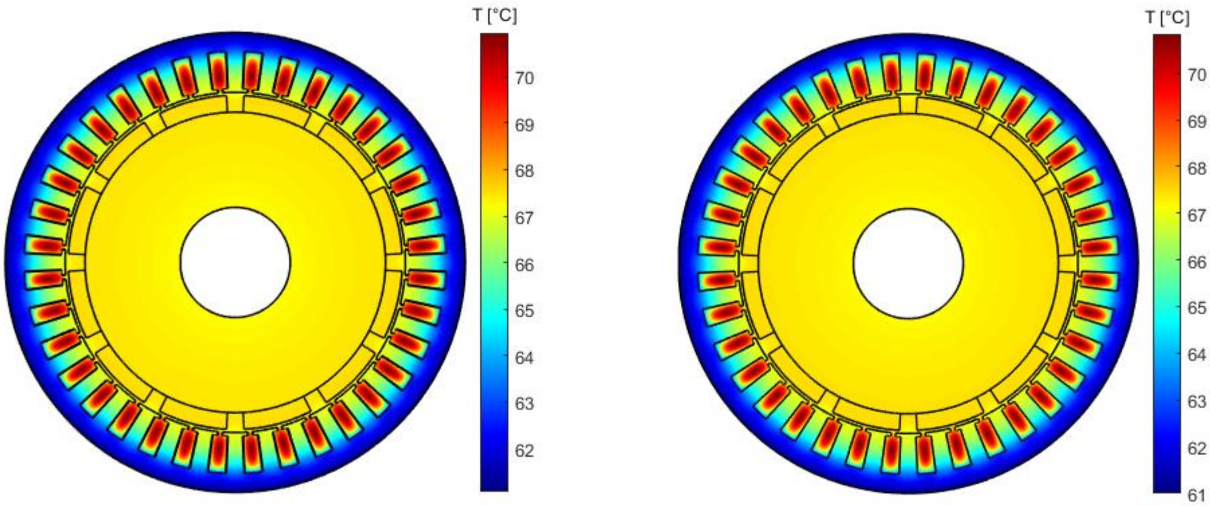

(a) (b)

Fig. 6. The level of temperature distribution in the PMSM: (a) Analytical, and (b) FEM.

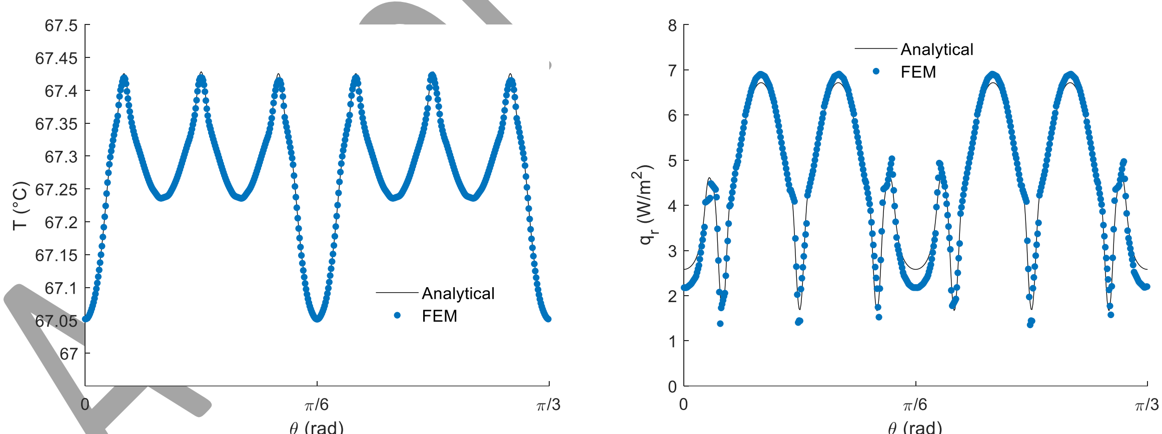

(a) (b)

DOI: 10.1108/COMPEL-07-2021-0226

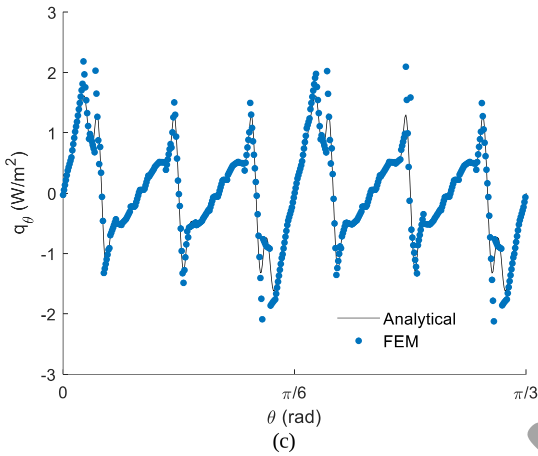

(c)

Fig. 7. Temperature and heat flux component distribution in the middle of air-gap: (a) Temperature, (b) Radial flux, and (c) Tangential flux.

The level of temperature distribution in the PMSM obtained by the developed analytical model and FEM is shown in **Fig. 6.** It can be observed that most of the heat is located in the stator slots. In the rotor yoke, PMs and air-gap, the temperature is approximately equal in each region. The area of lowest temperature in the PMSM is the stator yoke. This result is very reasonable, because most of the losses are located in the stator slots. The convection coefficient inside the rotor is very low, equal to 3 W/(m².K) (i.e., without cooling on this side), so the heat is trapped in the rotor although the losses in this part are low. For the stator yoke, the cooling effect is obvious because the convection coefficient outside the stator is very high. Moreover, the analytical results are very similar to those obtained by FEM.

The temperature and heat flux component distribution in the middle of air-gap is shown in **Fig. 7**. The analytical results are very similar to those from the FEM. The temperature is very stable in the air-gap [see **Fig. 7(a)**], varying by 0.4°C in the θ-direction. This result is confirmed by the tangential heat flux component [see **Fig. 7(c)**], where this value of q_θ is very small and reaches at ± 2 W/m² (i.e., the tangential heat flux component is obtained from the derivation of temperature versus θ). In **Fig. 7(b)**, the small error of 0.5 W/m² appears at $\theta = \{0, \pi/6, \pi/3\}$. This is not significant because the value of q_r is very small, which may exceed its value in some case to 10^4 W/m². The radial heat flux component is obtained from the derivation of temperature versus r. The positive value of q_r means that the temperature in the air-gap is decreasing in the r-direction, the reverse in the other case where q_r is negative. In the cases of small value of q_r, this means that the temperature is stable in the r-direction and the change is almost negligible. This corresponds perfectly to the case shown in **Fig. 7(b)**.

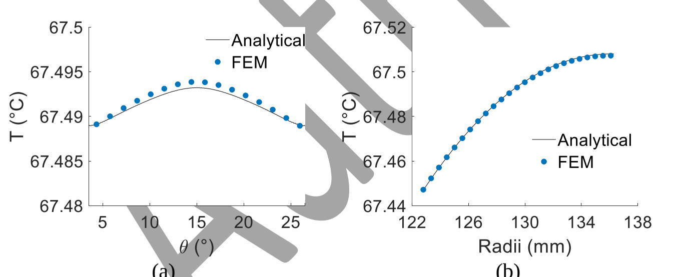

(a) (b)

Fig. 8. Temperature in the middle of the 1st PM in the: (a) θ-, and (b) r-direction.

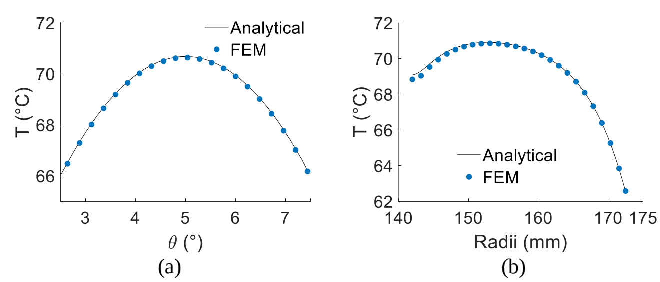

(a) (b)

Fig. 9. Temperature in the middle of the 1st stator slot-opening in the: (a) θ-, and (b) r-direction.

The temperature curves obtained analytically in the 1st PM and 1st stator slot-opening presented in the θ- and r-direction are given in **Figs. 8-9** and compared with FEM. The results are in very good agreement between the analytical model and FEM. In **Fig. 8**, the temperature distribution in the PM is stable with a small change in the r-direction where it increases in this direction. The reason is that the heat source in the PMSM comes from the stator. The PM eddy-current losses are very low due to the distribution winding type. In the stator slot [see **Fig. 9**], the heat is concentrated in the middle and decreases in the r-direction, because there is cooling in that direction outside the stator.

COMPEL: The International Journal for Computation and Mathematics in Electrical and Electronic Engineering
DOI: 10.1108/COMPEL-07-2021-0226

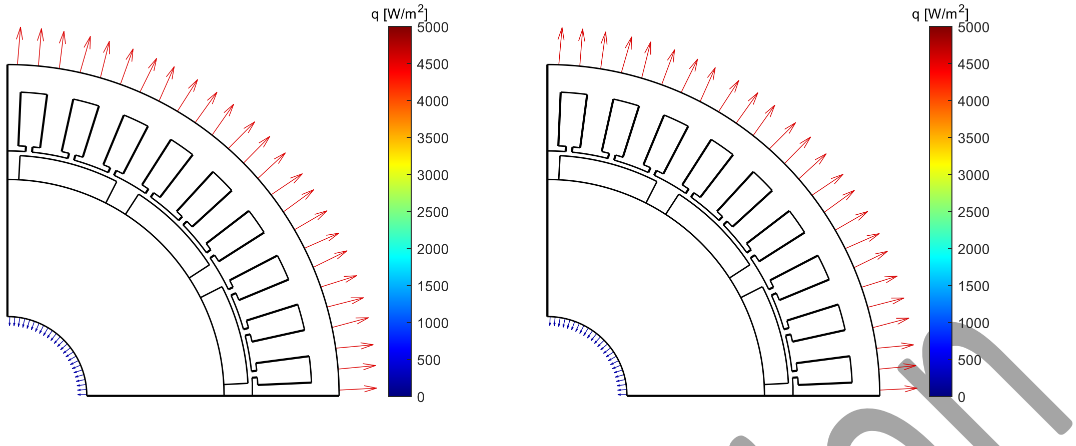

(a) (b)

Fig. 10. Heat flux inside and outside the PMSM (1/4 of the machine) represented by level and direction of arrow: (a) Analytical, and (b) FEM.

TABLE VII
DISSIPATIVE HEAT POWER FROM THE PMSM.

Power in (W)	P_{int}	P_{ext}	$P_{int} + P_{ext}$	P_{loss}
Analytical	16.71	1665.60	1682.31	1680.85
FEM	16.57	1665.54	1682.11	

In **Fig. 10**, the heat flux inside the rotor and outside the stator of PMSM is represented by arrows. The level of heat flux is presented by the color and size of the arrows. The maximum value of the heat flux outside the stator reaches q = 4,553 W/m² and inside the rotor is equal to q = 190 W/m². It can be seen that the direction of heat flux is directly out of PMSM in both the rotor and stator parts. The most of heat is extracted from the stator part due to the presence of cooling system on this side and the high value of losses in the stator, where this dissipative heat power is equal to 1665.6 W [see **Table. VII**], which represent 99 % of the extracted power from the PMSM. In **Table. VII**, it can be observed that the total extracted power from the PMSM, viz., $P_{int} + P_{ext}$, is almost equal to the total losses in the PMSM, viz., P_{loss}. Both results in **Fig. 10** and **Table. VII** of the analytical model and FEM are in good agreement.

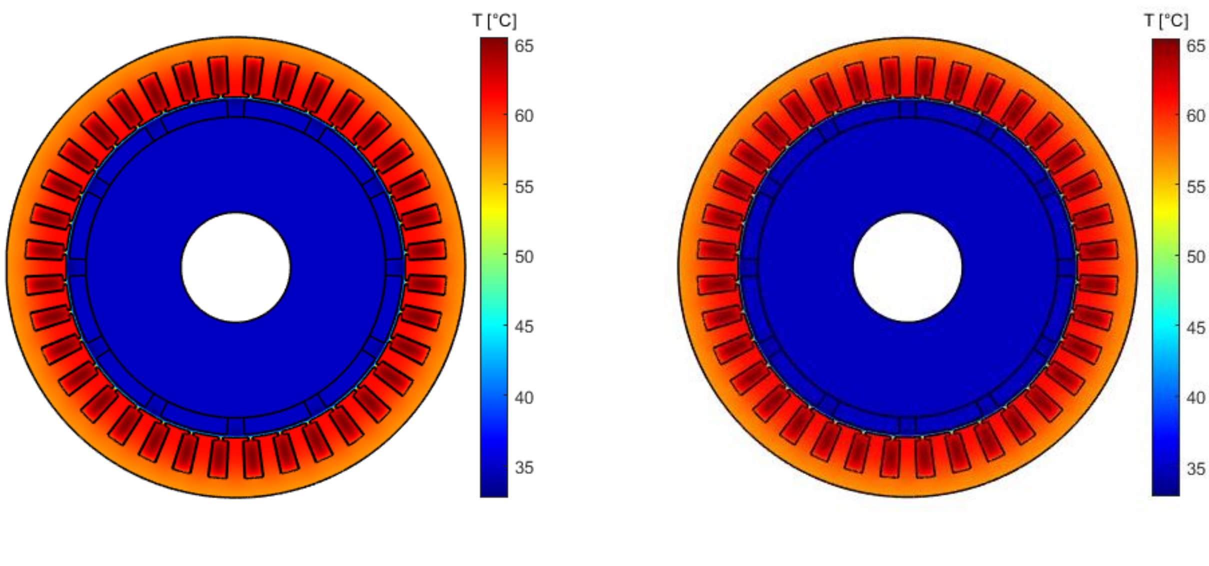

(a) (b)

Fig. 11. The level of temperature distribution in the PMSM with air-gap cooling: (a) Analytical, and (b) FEM.

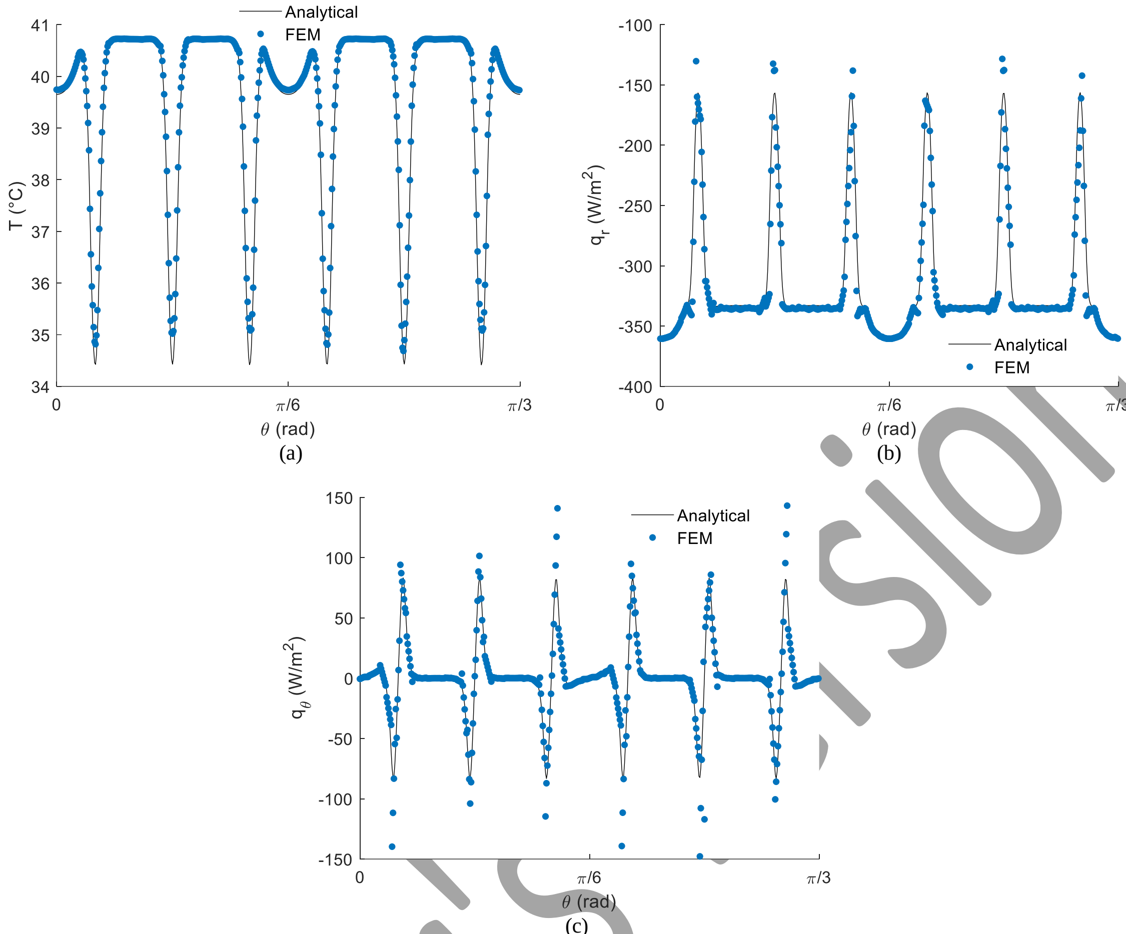

Fig. 12. Temperature and heat flux component distribution with cooling in the middle of air-gap. (a) Temperature, (b) Radial flux, and (c) Tangential flux.

In addition to cooling outside stator, the air-gap cooling can also be applied. This type of cooling can be modeled by applying a negative power in the air-gap. **Fig. 11** represent the level of temperature distribution where, in addition to the cooling applied to the outside of the stator, the power absorbed by cooling applied in the air-gap is equal to 200 W (i.e., ≅0.3 MW/m^3). This value is added in **(18)** (i.e., p_{co}=-200W in **Table. IV**). A good cooling of PMSM can be seen in **Fig. 11**, especially in the critical parts of the electrical machine. **Fig. 12(a)** represents the temperature in the air-gap which is lower than 41°C, where by comparison with **Fig. 7(a)**, a difference of 26.6°C can be observed. **Fig. 12(b)** gives the results of q_r in the air-gap where its value is negative. This means that the temperature in the air-gap increases in the r-direction. **Fig. 13** provides more details on the temperature change caused by the air-gap cooling. The temperature is decreased by 33°C in the PM and 5.5°C in the stator slot from 0 to 200 W of the power absorbed by cooling. All results of the numerical and analytical method are identical. This makes the developed model able to predict the temperature in electrical machines with different cooling condition.

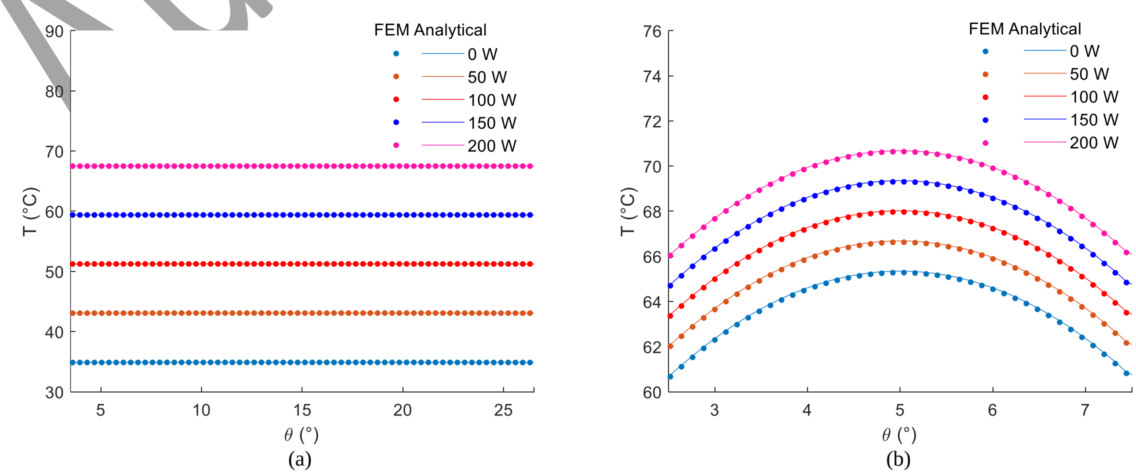

Fig. 13. Temperature with varying the absorbed power by cooling at the center of the 1st (a) PM and (b) stator slot.

COMPEL: The International Journal for Computation and Mathematics in Electrical and Electronic Engineering
DOI: 10.1108/COMPEL-07-2021-0226

In **Figs. 14 - 19**, a parametric study has been performed. It can be observed that the effect mode of the temperature variation in the elements of stator and rotor parts is different. This means that the air-gap separates them. The cooling outside the stator affects all parts of PMSM [see **Fig. 14**], where the temperature decreases by about 191°C from h_s= 5 W/(m².K) without cooling to h_s= 105 W/(m².K) with cooling. However, the application of cooling inside the rotor [see **Fig. 15**] cannot give a good result compared to the result of cooling outside the stator, because the two things, which have already been mentioned before, the majority of heat source are concentrated in the stator part and the role of the air-gap which represents a thermal insulator between the stator and the rotor parts. In **Fig. 16** and **17**, the emissivity variation does not significantly affect, however, their effect is important. The emissivity outside the stator decreases the temperature in all parts of PMSM with linearly, contrary with the emissivity inside the rotor where the influence on the temperature is affected only in the rotor parts [see **Fig. 17**]. The influence of temperature by the variation of absorbed power by cooling applied in the air-gap is presented in **Fig. 18**. A linearly variation form of temperature can be seen in all parts of PMSM and the heat trapped in the rotor has also been released. However, the cooling in the stator parts is good including the stator slots. Finally, **Fig. 19** represents the influence of the air-gap thermal conductivity on the temperature of PMSM. There is a very small change in the temperature of the PM and the rotor yoke. However, there are no significant differences between a good thermal conductor or a good thermal insulator in the air-gap (i.e., 30 and 0.03 W/(m.K)). The comparison of the parametric study results by analytical method and those obtained by FEM confirms the validity of the proposed analytical method to analyze and/or to predict the temperature distribution in the PMSM with a very good accuracy.

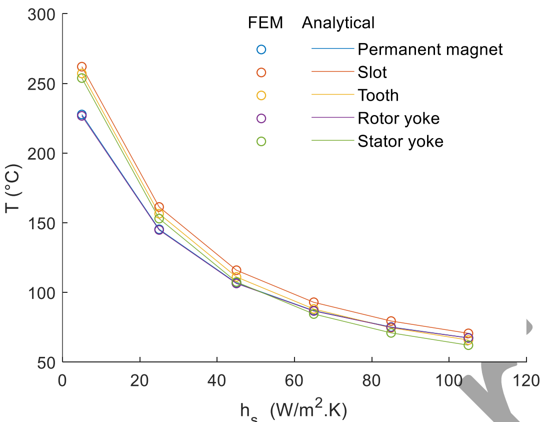

Fig. 14. Temperature variation with varying h_s and h_r = 3 W/(m2 ·K) in a point at the center of different parts of PMSM.

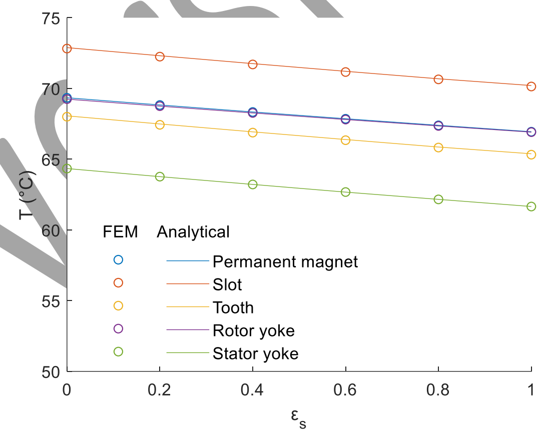

Fig. 16. Temperature variation with varying ε_s and ε_r= 0.2 in a point at the center of different parts of PMSM.

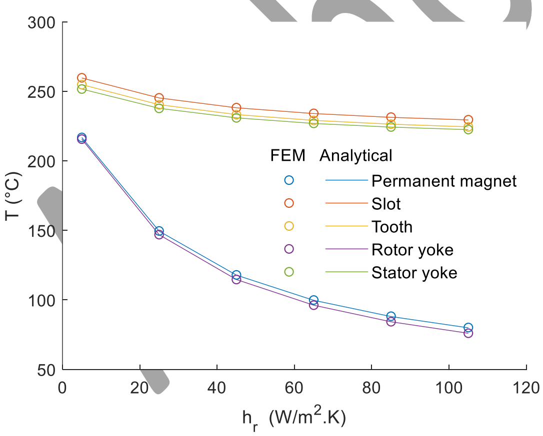

Fig. 15. Temperature variation with varying h_r and h_s = 5 W/(m2 ·K) in a point at the center of different parts of PMSM.

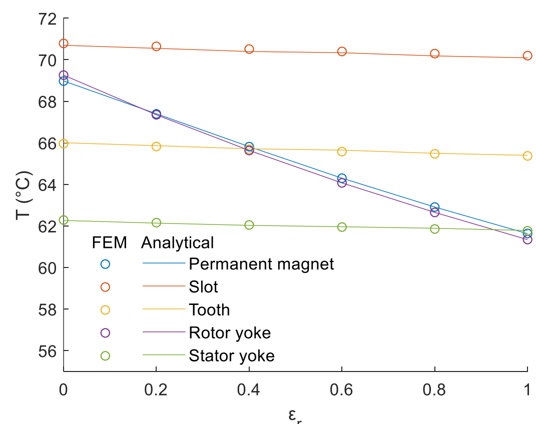

Fig. 17. Temperature variation with varying ε_r and ε_s= 0.8 in a point at the center of different parts of PMSM.

DOI: 10.1108/COMPEL-07-2021-0226

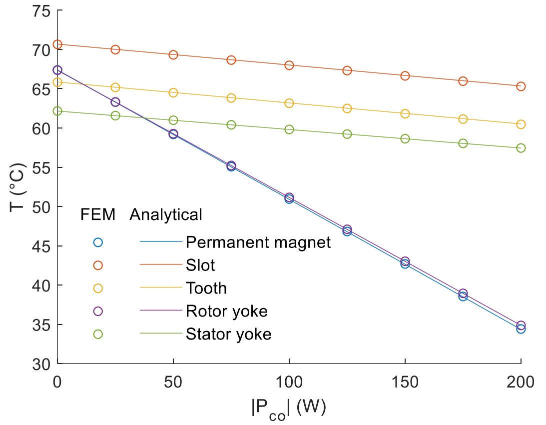

Fig. 18. Temperature variation with varying the absorbed power by cooling applied in the air-gap P_{co} in a point at the center of different parts of PMSM.

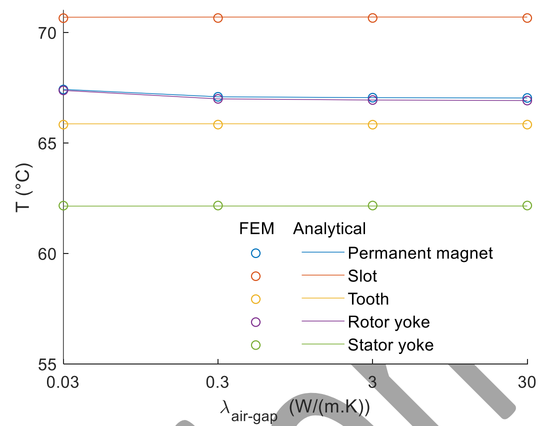

Fig. 19. Temperature variation with varying λ_a in a point at the center of different parts of PMSM.

VII. Conclusion

In this paper, the authors proposed a 2-D analytical model of steady-state temperature and heat flux components in PMSM. It is based on the multi-layer models with the convolution theorem (i.e., Cauchy's product theorem) by using the separation of variables method. Six regions are established. All the Laplace's and Poisson's equations are solved analytically where these equations are completely defined in terms of complex Fourier's series. The BCs inside the electrical machine are obtained from the continuity of temperature and radial heat-flux density at the interface. Then, the heat transfer by convection and radiation outside the electrical machine are applied, where any iterative method solves efficiently and takes into account the heat transfer by radiation. The model is validated by FEM for different conditions with excellent accuracy. It can be used for an optimization process that includes the effect of different cooling type or a parametric study by varying different important parameters such as the heat source or thermal conductivities of different parts of PMSM. Whereas, the analytical method has the advantage of a fast calculation time compared to FEM. In the same time, the analytical method has the disadvantage of not being able to model complex geometries. Although there is a way to solve this problem by adding more layers in the developed model.

In addition, it should be noted that one can introduce the nonlinear characteristic of thermal conductivity, which varies with temperature $\lambda(T)$ according to **0)** where is similar to the $B(H)$ curve. Moreover, to introduce the heat source directly into the proposed thermal model, the model must be coupled with an analytical model to predict the iron core losses [e.g., coupled with the model presented in **Djelloul-Khedda *et al.*, (2019)**]. However, to improve the results of the proposed model in order to take into account the end effect, an axial 2D model (i.e., x-y coordinate) by using the presented method should be develop by which the temperature in the final windings can be calculated.

Appendix A

The volumes of different parts of source heat are given by

$$\begin{cases} V_{ry} = L_u\pi(R_2^2 - R_1^2) \\ V_m = L_u p\theta_m(R_3^2 - R_2^2) \\ V_a = L_u\pi(R_4^2 - R_3^2) \\ V_t = \dfrac{L_u Q_s}{2}[\theta_t(R_6^2 - R_5^2) + \theta_{ts}(R_5^2 - R_4^2)] \\ V_{sl} = \dfrac{L_u Q_s \theta_s}{2}(R_6^2 - R_5^2) \\ V_{sy} = L_u\pi(R_7^2 - R_6^2) \end{cases} \tag{A.1}$$

where V_{ry}, V_m, V_a, V_t, V_{sl} and V_{sy} are respectively the volume of the rotor yoke, all PMs, the air-gap, all teeth including tooth-tips, all stator slot and the stator yoke.

Appendix B

The radii of different regions used in the developed analytical model can be calculated from the parameter's geometry according to **Table I** by the following formulas

$$\begin{cases} R_1 = R_{sh} \\ R_2 = R_1 + h_{ry} \\ R_3 = R_2 + h_m \\ R_4 = R_3 + h_g \\ R_5 = R_4 + h_p \\ R_6 = R_4 + h_{sl} \\ R_7 = R_6 + h_{sy} \end{cases} \tag{B.1}$$

Appendix C

The external and internal column vectors of ambient temperature $\{\mathbf{T}_{int};\ \mathbf{T}_{ext}\}$ are given by

$$\mathbf{T}_{ext} = \begin{bmatrix} \hat{T}_{ext_{-N}} & \cdots & \hat{T}_{ext_N} \end{bmatrix}^T \tag{C.1}$$

$$\mathbf{T}_{int} = \begin{bmatrix} \hat{T}_{int_{-N}} & \cdots & \hat{T}_{int_N} \end{bmatrix}^T \tag{C.2}$$

$$\hat{T}_{amb,n} = \begin{cases} \displaystyle\sum_{i=1}^{Q/\tau} \frac{1}{2\pi jn} \left[T_{amb,T} e^{-jn\tau\frac{\theta_S}{2}} \left(1 - e^{-jn\tau\theta_t T}\right) + 2jT_{amb,S} \sin\left(\frac{n\tau\theta_S}{2}\right) \right] e^{jn\tau\alpha_i}, & n \neq 0 \\ \dfrac{Q}{2\pi} \left(T_{amb,T}\theta_T + T_{amb,S}\theta_S\right), & n = 0 \end{cases} \tag{C.3}$$

where $\{\hat{T}_{amb,n}, Q, T_{amb,T}, T_{amb,S}, \theta_T, \theta_S, \alpha_i, i\}$ are replaced by $\{\hat{T}_{int,n}, Q_s, T_{int}, T_{int}, \theta_t, \theta_s, \alpha_i, i\}$ for the internal ambient temperature and by $\{\hat{T}_{ext,n}, Q_s, T_{ext}, T_{ext}, \theta_t, \theta_s, \alpha_i, i\}$ for the external ambient temperature.

Appendix D

The equivalent thermal conductivity of air-gap λ_a is calculated corresponding to (Ball *et al.*, 1989) by

$$\lambda_a = \beta\, \eta^{-2.9084}\, R_e^{0.4614\ \ln(3.3361\eta)} \tag{D.1}$$

$$R_e = R_3 h_g \frac{\omega_r}{\upsilon_0} \tag{D.2}$$

where β is experience factor considering surface roughness of rotor; $\eta = R_3/R_4$; R_3 is rotor outer radius; R_4 is stator inner radius; R_e is Reynolds number; h_g is air-gap length; and υ_0 is air kinematic viscosity.

References

Adouni A. and Cardoso, A. J. M. (2019), "Thermal Analysis of Synchronous Reluctance Machines-A Review", *Electric Power Components and Systems,* Vol. 47, Nos. 6-7, pp. 471-485.

Ball, K. S., Farouk, B. and Dixit, V. C. (1989) ''An experimental study of heat transfer in a vertical annulus with a rotating cylinder", *International Journal of Heat and Mass Transfer,* Vol. 32, No. 8, pp 1517-1527.

Benlamine, R., Dubas. F., Randi, S-A., Lhotellier, D. and Espanet, C. (2015), "3-D numerical hybrid method for PM eddy-current losses calculation: Application to axial-flux PMSMs", *IEEE Transactions on Magnetics*, Vol. 51, No. 7.

Bertotti, G. (1988), "General properties of power losses in soft ferromagnetic materials", *IEEE Transactions on Magnetics*, Vol. 24, No. 1, pp. 621-630.

Boglietti, A., Cavagnino, A., Staton, D., Shanel, M., Mueller, M. and Mejuto, C. (2009), "Evolution and modern approaches for thermal analysis of electrical machines", *IEEE Transactions on Industrial Electronics*, Vol. 56, No. 3, pp. 871-882.

Boughrara, K. and Dubas, F. (2021), "2-D steady-state heat transfer prediction in rotating electrical machines taking into account materials anisotropy: Thermal resistances network, exact analytical and hybrid methods", *ENP Engineering Science Journal,* Accepted.

Boughrara, K., Ibtiouen, R. and Lubin, T. (2012), "Analytical prediction of magnetic field in parallel double excitation and spoke-type permanent-magnet machines accounting for tooth-tips and shape of polar pieces", *IEEE Transactions on Magnetics,* Vol. 48, No. 7, pp. 2121-2137.

Boughrara, K., Dubas, F. and Ibtiouen, R. (2018), "2-D exact analytical method for steady-state heat transfer prediction in rotating electrical machines", *IEEE Transactions on Magnetics,* Vol. 54, No. 9.

Buyukdegirmenci, V.T., Magill, M.P., Nategh, S. and Krein, P.T. (2013a), "Development of closed-form solutions for fast thermal modeling of rotating electric machinery", in Proc. IEMDC, Chicago, IL, USA, pp. 832-838.

Buyukdegirmenci, V.T., Nategh, S., Magill, M.P. and Krein, P.T. (2013b), "A fast and flexible analytical approach for thermal modeling of a linear stator structure", in Proc. IEMDC, Chicago, IL, USA, pp. 793-800.

Chang, H.-Y.H., Yang, Y.-P. and Lin, F.K.-T. (2017), "Thermal-fluid and electromagnetic coupling analysis and test of a traction motor for electric vehicles", *Journal of the Chinese Institute of Engineers,* Vol. 41, No. 1, pp. 51–60.

Chong, Y.C. (2015), "Thermal analysis and air flow modelling of electrical machines", Ph.D. dissertation, University of Edinburgh, Edinburgh, U.K.

Djelloul-Khedda, Z., Boughrara, K., Dubas, F. and Ibtiouen, R. (2017), "Nonlinear analytical prediction of magnetic field and electromagnetic performances in switched reluctance machines", *IEEE Transactions on Magnetics,* Vol. 53, No. 7.

Djelloul-Khedda, Z., Boughrara, K., Dubas, F., Kechroud, A. and Tikellaline, A. (2019), "Analytical prediction of iron-core losses in flux-modulated permanent-magnet synchronous machines", *IEEE Transactions on Magnetics,* Vol. 55, No. 1.

Dong, B., Wang, K., Han, B. and Zheng, S. (2019), "Thermal analysis and experimental validation of a 30 kW 60000 r/min high-speed permanent magnet motor with magnetic bearings", *IEEE Access*, Vol. 7, pp. 92184-92192.

Dubas F. and Boughrara, K. (2017a), "New scientific contribution on the 2-D subdomain technique in Cartesian coordinates: Taking into account of iron parts", *Mathematical and Computational Applications,* Vol. 22, No. 1, p. 17.

Dubas F. and Boughrara, K. (2017b), "New scientific contribution on the 2-D subdomain technique in polar coordinates: Taking into account of iron parts", *Mathematical and Computational Applications,* Vol.22, No. 4, p. 42.

Dubas F. and Espanet, C. (2009), "Analytical solution of the magnetic field in permanent-magnet motors taking into account slotting effect: No-load vector potential and flux density calculation", *IEEE Transactions on Magnetics,* Vol. 45, No. 5, pp. 2097-2109.

Ghahfarokhi, P.S., Kallaste, A., Belahcen, A., Vaimann, T. and Rassolkin, A. (2016), ''Review of thermal analysis of permanent magnet assisted synchronous reluctance machines'', in Proc. PQ., Tallinn, Estonia, pp. 219-224.

Grobler, A.J., Holm, S.R. and van Schoor, G. (2013), "Thermal modelling of a high speed permanent magnet synchronous machine", in Proc. IEMDC, Chicago, IL, USA, pp. 319-324.

Grobler, A.J., Holm, S.R. and van Schoor, G. (2015), "A two-dimensional analytic thermal model for a high-speed PMSM magnet", *IEEE Transactions on Industrial Electronics,* Vol. 62, No. 11, pp. 6756–6764.

Hosain, M.L., Fdhila, R.B. and Rönnberg, K. (2017), "Air-gap flow and thermal analysis of rotating machines using CFD", *Energy Procedia,* Vol. 105, pp. 5153-5159.

Jiang, W. and Jahns, T.M. (2015), "Coupled electromagnetic–thermal analysis of electric machines including transient operation based on finite-element techniques", *IEEE Transactions on Industrial Electronics,* Vol. 51, No. 2, pp. 1880-1889.

Li, S., Sarlioglu, B., Jurkovic, S., Patel, N.R. and Savagian, P. (2017), "Analysis of temperature effects on performance of interior permanent magnet machines for high variable temperature applications", *IEEE Transaction on Industrial Application,* Vol. 53, No. 5, pp. 4923-4933.

Meeker, D.C., (2010), "Finite element method magnetics", *Version 4.2, Build,* available at: http://www.femm.info.

Nasab, P.S., Perini, R., Gerlando, A.D., Foglia, G.M. and Moallem, M. (2020), ''Analytical thermal model of natural-convection cooling in axial flux machines", *IEEE Transactions on Industrial Electronics,* Vol. 67, No. 4, pp. 2711-2721.

Nategh, S., Zhang, H., Wallmark, O., Boglietti, A. Nassen, T. and Bazant, M. (2019), ''Transient thermal modeling and analysis of railway traction motors", *IEEE Transactions on Industrial Electronics,* Vol. 66, No. 1, pp. 79-89.

Nategh, S., Huang, Z., Krings, A., Wallmark, O. and Leksell, M. (2013), "Thermal modeling of directly cooled electric machines using lumped parameter and limited CFD analysis", *IEEE Transactions on Energy Conversion,* Vol. 28, No. 4, pp. 979-990.

Nategh, S., Wallmark, O., Leksell, M. and Zhao, S. (2012), "Thermal analysis of a PMaSRM using partial FEA and lumped parameter modeling", *IEEE Transactions on Energy Conversion, Vol*. 27, No. 2, pp. 477-488.

Sprangers, R.L.J., Paulides, J.J.H., Gysen, B.L.J. and Lomonova, E.A. (2016), "Magnetic saturation in semi-analytical harmonic modeling for electric machine analysis", *IEEE Transactions on Magnetics,* Vol. 52, No. 2.

Wang, A., Li, H. and Liu, C. (2008), "On the material and temperature impacts of interior permanent magnet machine for electric vehicle applications", *IEEE Transactions on Magnetics,* Vol. 44, No. 11, pp. 4329-4332.

Wang, J., Hu, Y., Cheng, M., Li, B. and Chen, B. (2020), "Bidirectional coupling model of electromagnetic field and thermal field applied to the thermal analysis of the FSPM machine", *Energies*, vol. 13, no. 12, p. 3079.

Yang, Y., Bilgin, B., Kasprzak, M., Nalakath, S., Sadek, H., Preindl, M., Cotton, J., Schofield, N. and Emadi, A. (2017), "Thermal management of electric machines", *IET Electrical Systems in Transportation,* vol. 7, no. 2, pp. 104-116.

Zhang, G., Hua, W., Cheng, M., Zhang, B. and Guo, X. (2017), "Coupled magnetic-thermal fields analysis of water cooling flux-switching permanent magnet motors by an axially segmented model", *IEEE Transactions on Magnetics,* Vol. 53, No. 6.

Zhang, H., Giangrande, P., Sala, G., Xu, Z., Hua, W., Madonna, V., Gerada, D. and Gerada., C. (2021), ''Thermal model approach to multisector three-phase electrical machines", *IEEE Transactions on Industrial Electronics,* Vol. 68, No. 4, pp. 2919-2930.